

DESIGN AND EXPERIMENTAL IMPLEMENTATION OF A
QUASI-DIRECT-DRIVE LEG FOR OPTIMIZED JUMPING

Draft of June 11, 2017 at 11:27

BY

YANRAN DING

THESIS

Submitted in partial fulfillment of the requirements
for the degree of Master of Science in Mechanical Science and Engineering
in the Graduate College of the
University of Illinois at Urbana-Champaign, 2017

Urbana, Illinois

Adviser:

Hae-Won Park

ABSTRACT

Input your text here

Draft of June 11, 2017 at 11:27

To my parents, for their love and support.

ACKNOWLEDGMENTS

Input your text here

TABLE OF CONTENTS

LIST OF TABLES	vi
LIST OF FIGURES	vii
LIST OF ABBREVIATIONS	ix
CHAPTER 1 INTRODUCTION	1
1.1 Motivation	2
1.2 Contribution	4
1.3 Thesis Outline	4
CHAPTER 2 SYSTEM MODELING	5
2.1 System Modeling	5
CHAPTER 3 SENSITIVITY ANALYSIS	14
3.1 Poincaré Map	14
3.2 Periodic Orbits	14
3.3 Monodromy Matrix	14
CHAPTER 4 DESIGN PRINCIPLES FOR DYNAMIC LEGGED ROBOTS	16
4.1 Transmission Design	16
4.2 Leg Topology Comparison	19
CHAPTER 5 HARDWARE INTEGRATION	30
5.1 Mechanical Design of The Leg	30
REFERENCES	34

LIST OF TABLES

4.1 Variable Definition for Gear Ratio Calculation	18
--	----

LIST OF FIGURES

1.1	A squirrel leaping forward (up) The robot leg presented in this leaping forward (bottom)	4
2.1	Sequential design process for determining design parameters. (a) knee extensor model for motor selection (b) detailed leg model for linkage design and gear ratio choice (c) hardware platform for experiments	6
2.2	Maximal achievable height for specific torque and speed limit. The x-axis corresponds to maximal angular velocity of the actuator, the y-axis corresponds to maximal torque of the actuator, and the depth represents the maximal achievable height of a jump	11
2.3	The Admissible Operating Region (AOR) formed by the torque and angular speed trajectories from the one hundred knee extensor model simulations. A typical motor's speed-torque curve scaled by gear ratio of 23:1 is plotted in green curve. Hip motor acts as a passive joint throughout the jumping up phase.	12
4.1	Schematics of Compound Planetary Gearbox Configurations. (left) 2 planet configuration, (right) 3 planet configuration	17
4.2	Three typical linkage topologies (a)Open-serial chain (b)Parallel five-bar (c)Symmetric five-bar. The design variable is δ and the workspace variable is the leg's radial extension	20
4.3	Force production in radial direction for an example linkage design of Open-chain, Parallel five-bar and Symmetric five-bar	22
4.4	Force production in radial and lateral directions for open chain design	22
4.5	Force production in radial and lateral directions for parallel five-bar design	23
4.6	Force production in radial and lateral directions for symmetric five-bar design	23

4.7	Velocity production in radial direction for an example linkage design of Open-chain, Parallel five-bar and Symmetric five-bar	24
4.8	Velocity production in radial and lateral directions for open chain design	24
4.9	Velocity production in radial and lateral directions for parallel five-bar design	25
4.10	Velocity production in radial and lateral directions for symmetric five-bar design	25
4.11	Proprioceptive Sensitivity in radial direction for an example linkage design of Open-chain, Parallel five-bar and Symmetric five-bar	26
4.12	Proprioceptive Sensitivity in radial and lateral directions for the open-chain design	27
4.13	Proprioceptive Sensitivity in radial and lateral directions for the parallel five-bar design	27
4.14	Proprioceptive Sensitivity in radial and lateral directions for the symmetric five-bar design	28
5.1	Planetary gearbox design with three compound planet gears (left); curved upper-link design (middle); hip and knee motor module (right); (1) sun gear, (2) compound planet gear, (3) ring gear, (4) stand-off, (5) brass dowel pin, (6) output pin, (7) upper link, (8) KNEE carrier, (9) KMF PBXS020 bearing, (10) the KNEE motor module	31
5.2	CAD Model of the Leg Module Design; (left) A side-view of the leg module with cut-out on thigh link showing the four-bar linkage design; (right) A cut-out view showing the internal structure of a motor module	31
5.3	(left) Connection Design Between HIP and KNEE Motors for Large Hip Range of Motion (ROM); (right) Exploded View of ABAD motor	32

LIST OF ABBREVIATIONS

CHAPTER 1

INTRODUCTION

The last century has seen great advancement of human transportation technology. whether it be wheeled vehicles running on the road, or submarines cruising the depth of seas, or rockets exploring the outer space. Human have not only conquered the land, but also the ocean, and even the space by enhancing our mobility using advanced vehicles. While these vehicles are fast, efficient and far-reaching, they all need highly structured media to work well. The Earth's most unstructured terrain still haven't seen the modern machinery of mankind. For example, the Amazon rain forest has remained mysterious for its dense branches have baffled even the most advanced of man-made machine. However, small and agile animals such as squirrels can perform highly dynamic maneuvers and move freely in highly unstructured environment.

In addition to running fast, climbing trees, squirrels are capable of jumping from branch to branch because of its small size and long jumping distance, which spans for around one meter. Squirrels could perform these powerful jumps using its short limbs and position its foot accurately for landing. This highly dynamic and agile movement is unparalleled in conventional vehicles. That is the reason why scientists devote decades to study the movement of agile animals such as squirrels and robotists draws inspiration from nature to create robotic counterparts.

Current state-of-art robots are becoming more agile with higher capability to interact with complicated environment. Boston Dynamics have recently developed robots such as BigDog, Spot and SpotMini, Atlas and Handle have demonstrated impressive progress made in legged robots. Quadrupedal robots made by Boston Dynamics could not only walk and climb stairs but also run, bound and recover rapidly from external push or slippage. Other robots such as MIT Cheetah[15] has demonstrated remarkable traits of high speed bounding and ability to jump over high obstacles. Minitaur from

University of Pennsylvania[13] has shown that small robots could perform highly agile motions like running, hopping and transversing uneven terrain. An additional advantage of small robots is that they could maneuver in tight space.

1.1 Motivation

Wheeled vehicles are widely used for transportation, but they cannot reach places with unstructured terrain. In contrast, human and animals are able to access these places using legs. While legged locomotion is not as efficient as wheeled one, it certainly possesses advantage in overcome large and complex obstacles and traversing unstructured land. This is especially useful in disaster scenarios where there are a lot of debris and collapsed structures. For example, in the Fukushima nuclear disaster happened in March 2011, no robots were able to reach the most damaged area let alone do inspection and repairing. This disastrous accident has since called attention to robot development. Defense Advanced Research Project Agency (DARPA) organized a robotic challenge which assembled teams with the most advanced robots at that time to perform disaster relief related tasks. These robots are delicate and complicated machines designed by talented robotists all over the world. Furthermore, advanced control algorithm were employed. In spite of the brilliance imbued in the robots, the robots' motion was slow and by no means dynamic.

In order to achieve robust locomotion in the real world, legged robots should be able to interact with the environment. In addition, the robot should also be able to achieve multiple modes of locomotion. It should be able to move fast and dynamically in structured terrain by employing running gait; and move cautiously and slowly in unstructured terrain using advanced motion planning algorithm. In addition, the robot should be able to execute explosive motion such as jumping in face of large obstacles. This trait is very useful especially in disaster zones where there are a collapsed walls and floors which impedes the ways of the robot. In this situation, jumping motion could easily clear the obstacle.

In order to achieve such dynamic motion such as jumping, researchers have been drawing inspiration from nature. The squirrels is a small and

agile animal that can perform highly dynamic maneuvers. As could be seen in Figure 1.1, where a squirrel is jumping from a pole to a branch. It has to exert considerable amount of force in the jumping phase and balance its attitude during aerial phase and handle large impulse at touch-down moment.

Inspired by the athletic biological system, we investigated the dynamic motion generation scheme of small scale robots, specifically the jumping capability. It is observed in nature that animals with extremely different scales can achieve same magnitude jumping height, given they were geometrically similar [2]. However, smaller animals need to accelerate much faster and produce higher angular speed to reach the same take-off velocity [18]. This observation motivated our interest on how scaling of a robotic system would change the requirement on actuator characteristics. Analogy was drawn to legged robot design in the sense that an isometrically scaled down robot requires higher actuator speed to produce comparable dynamic motion [19].

Motor speed scarcity becomes a bigger problem in smaller sized robot design. Because if the linkage dimension scaled down by $\frac{1}{L}$ ($L > 1$), required motor speed is scaled by L to produce the same end-effector velocity. High torque density (torque per unit mass) is desirable for dynamic robotic systems [20], because actuators need to produce forces 2.6 to 3 times of body weight for high speed locomotion [21][4]. Heavily geared motors have high torque density at the cost of increased reflected inertia and friction[17], which compromises robustness because it is prone to break upon impact. Series elastic actuators (SEA) could produce variable mechanical impedance and recycle energy for high efficiency gait. However, their actuation bandwidth is limited [16]. Direct drive robots [3] do not use any speed reduction system, thus eliminate all the problems(backlash, friction, high reflected inertia) associated with gearboxes and possess the benefits of high transparency [5] and mechanical robustness. In addition, the absence of speed reduction excludes the possibility of speed scarcity. Nevertheless, low torque density, high motor weight and Joule heating are the main disadvantages of direct drive. Quasi-direct-drive actuator strategy [12] was employed in this work to balance amongst torque density, motor speed and impact force.

For dynamic locomotion, motors' torque and speed limit should both be taken into account for legged robot design in order to optimize the robot's performance. In this paper, we present the design and optimization process of a leg prototype. Major design decisions were made based on the hybrid

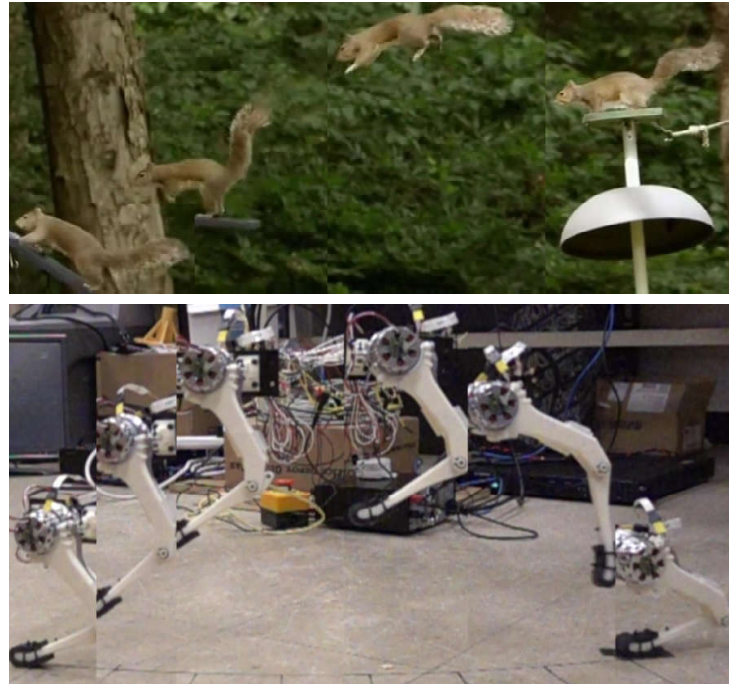


Figure 1.1: A squirrel leaping forward (up) The robot leg presented in this leaping forward (bottom)

approach of nonlinear optimization and manipulability analysis. Section ?? introduces the dynamic models for optimization. In Section ?? we describe the mechanical design process of the leg based on simulation and manipulability analysis. Section ?? demonstrates the jumping capability of the leg.

1.2 Contribution

1.3 Thesis Outline

CHAPTER 2

SYSTEM MODELING

2.1 System Modeling

A sequential and iterative design process was adopted to refine simulation model and mechanical design as shown in Figure 2.1. The 1-DOF template [8] called **knee extensor model** was used to investigate the torque and angular speed requirement of the leg, as depicted in Figure 2.1(a). It assumes all masses are lumped at the base; thigh and shank link are of same length and have no mass or inertia; foot is located directly below the hip, which means no horizontal off-set for foot hold. Jumping motion was simulated using this knee extensor model under various motors' maximal speed and maximal torque. These simulations in turn exposed the speed and torque requirements in order to achieve the desired motion, which provides guidance for choosing appropriate motor and gear ratio.

A more detailed leg model with motors' rotary inertia and horizontal foot off-set was introduced as shown in Figure 2.1 (b). The detailed leg model was used to further narrow the choice of gear ratio by minimizing ground impact force while maintaining balance between torque and speed requirements. Optimized parameters were tested on the hardware platform shown in Figure 2.1 (c) to validate the design.

2.1.1 Knee Extensor Model

The knee extensor model was used to estimate the torque and speed requirements to achieve desirable jumping motions, which provides us with an initial guidance for choosing motor and gearbox. Figure 2.1 (a) shows the schematics of the knee extensor model. The model assumes that all masses are lumped at the base to be M , which is mounted on a vertical linear rail.

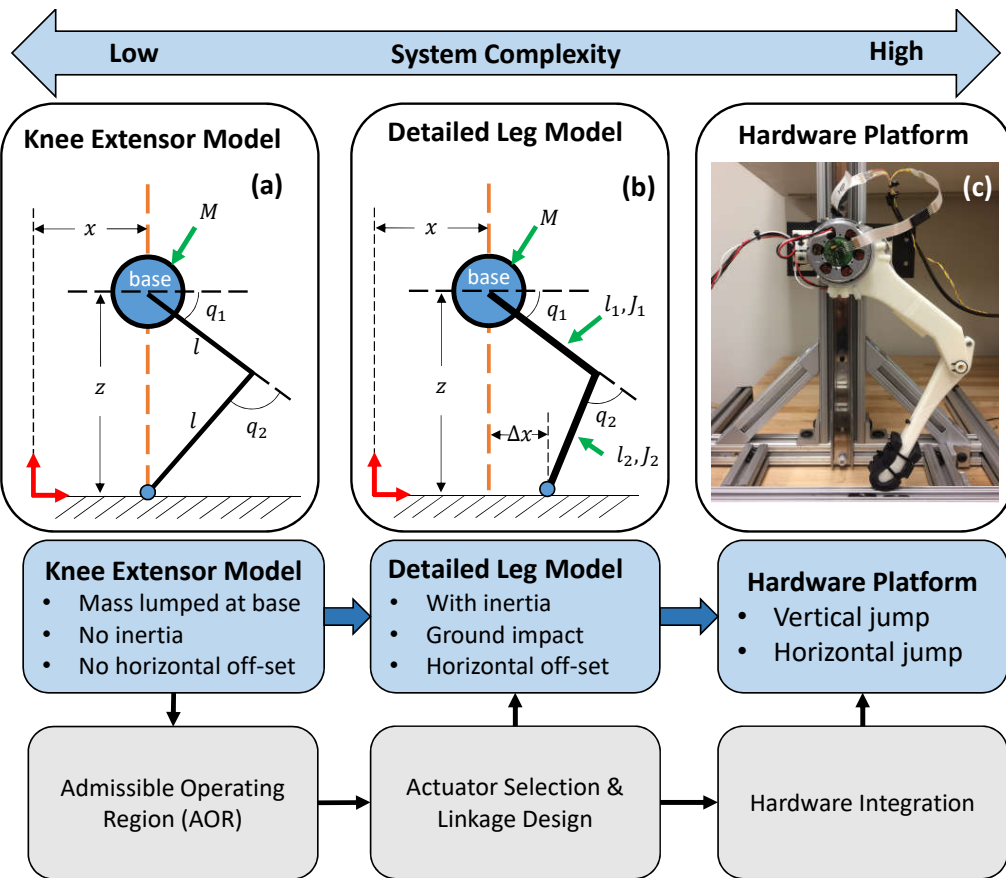


Figure 2.1: Sequential design process for determining design parameters.
 (a) knee extensor model for motor selection (b) detailed leg model for linkage design and gear ratio choice (c) hardware platform for experiments

Thigh and shank links have an identical length of l , while its foot and base are vertically aligned. Hence only the knee joint needs to be actuated to perform vertical jump while the hip joint is not actuated. The vertical height of the base z and joint angles q_1, q_2 are shown in Figure 2.1.

The dynamics of this model was formalized as a single point mass accelerated due to ground reaction force (GRF). Ground reaction force was chosen as the control input because it is the only external force in the knee extensor model that could increase the mechanical energy of the system. The equation of motion (EOM) of the system is: $\ddot{z} = \frac{F_z}{M} - g$, where z is the vertical displacement of the base, F_z is the vertical component of GRF, M is the lumped mass at the base and g is the gravitational acceleration.

2.1.2 GRF Parameterized as Bézier Polynomial

A 5th order Bézier polynomial was used to parameterize the GRF profile. The reasons for using Bézier Polynomial to parametrize the ground reaction force is two fold. Firstly, the first and last coefficient of a Bézier polynomial corresponds to the initial and final value of the GRF, which makes it more convenient to anchor GRF to desired values at the initial and final instance; secondly, integration of Bézier Polynomial is a linear operation, which is computationally inexpensive. This property is utilized in integrating the prescribed ground reaction force and integrate to get the velocity trajectory, as shown in Equation 2.4, and integrate again to get the position trajectory

The coefficients of Bézier polynomial are assumed to be $[Mg, \alpha_1, \alpha_2, \alpha_3, \alpha_4, 0]$. The first coefficient was set to be the weight of the leg because it is assumed that the leg starts from static equilibrium state, and last coefficient was set as 0 to ensure a smooth and physically feasible motion at the take-off moment.

The Bernstein polynomials are defined over $[0,1]$ as:

$$B_{i,N} = \binom{N}{i} x^i (1-x)^{n-i}, 0 \leq i \leq N \quad (2.1)$$

where $\binom{N}{i}$ is the binomial coefficients.

Since a Bézier polynomial is the linear combination of a Bernstein polynomial basis[6] defined as,

$$C_N(s) = \sum_{i=0}^N \alpha_i B_{i,N}(s) \quad (2.2)$$

where α_i is the coefficient for the i^{th} Bernstein polynomial $B_{i,N}$, analytical solution for velocity and position could be obtained using the property of the Bernstein polynomial[7]:

$$\frac{d}{ds} B_{i,N}(s) = \frac{N}{T} (B_{i-1,N-1}(s) - B_{i,N-1}(s)) \quad (2.3)$$

where s is a point between general time interval $[0, T]$.

Given the initial velocity \dot{z}_0 , the velocity trajectory in stance phase is a 6^{th} order Bézier polynomial with coefficients $\gamma_{(0-6)}$. The linear relationship between force and velocity Bézier coefficient is:

$$\frac{6}{T_{st}} \begin{bmatrix} -1 & 1 & 0 & 0 & 0 & 0 & 0 \\ 0 & -1 & 1 & 0 & 0 & 0 & 0 \\ 0 & 0 & -1 & 1 & 0 & 0 & 0 \\ 0 & 0 & 0 & -1 & 1 & 0 & 0 \\ 0 & 0 & 0 & 0 & -1 & 1 & 0 \\ 1 & 0 & 0 & 0 & 0 & 0 & 0 \end{bmatrix} \begin{bmatrix} \gamma_0 \\ \gamma_1 \\ \gamma_2 \\ \gamma_3 \\ \gamma_4 \\ \gamma_5 \\ \gamma_6 \end{bmatrix} = \begin{bmatrix} 0 \\ \alpha_1 \\ \alpha_2 \\ \alpha_3 \\ \alpha_4 \\ 0 \\ \dot{z}_0 \end{bmatrix} \frac{1}{M} - g \quad (2.4)$$

where T_{st} is the stance duration for jumping up.

Similarly, the position trajectory in stance phase could also be integrated by applying the linear operation shown in Equation 2.4 given initial position z_0 . At each instance $t \in [0, T_{st}]$, the joint angle $q = [q_1, q_2]$ defined in Figure 2.1(a) was solved by inverse kinematics.

Since the thigh and shank links are assumed to be massless, joint torque $\tau = [\tau_1, \tau_2]$ could be reconstructed using

$$\tau = J(q)^T F \quad (2.5)$$

where τ_1 and τ_2 are joint torques for hip and knee joints, F is the ground reaction force, and $J(q) \in R^{2 \times 2}$ is the manipulator Jacobian of the foot relative to the hip.

The jumping performance was evaluated by the maximal reachable height

h_{max} ,

$$h_{max} := h_{to} + \frac{v_{to}^2}{2g} \quad (2.6)$$

where h_{to} and v_{to} are the base height and speed at the moment of take-off.

2.1.3 Nonlinear Optimization for Ground Reaction Force

In order to get the optimal ground reaction force profile within actuator limits, an optimal control problem was formulated and solved using nonlinear optimization:

$$\begin{aligned} \min \quad & -h_{max} \\ s.t. \quad & q_{lb} \leq q \leq q_{ub} \\ & \dot{q}_{lb} \leq \dot{q} \leq \dot{q}_{ub} \\ & \tau_{lb} \leq \tau \leq \tau_{ub} \end{aligned} \quad (2.7)$$

where q_{lb} , q_{ub} are the lower and upper bounds for joint angles; \dot{q}_{lb} , \dot{q}_{ub} for angular velocity; τ_{lb} , τ_{ub} for joint torques.

Dynamics was discretized at N sampling points to search for optimal variable values. Joint angle q and angular velocity \dot{q} were discretized at the sampling points. Motor's maximal speed and torque constraints were imposed at each sampling point as inequality constraints.

The optimization variables are chosen as follows:

$$x_{opt} = [z_0, \alpha_{(1-4)}, T_{st}, q_{(1-N)}, \dot{q}_{(1-N)}] \quad (2.8)$$

where x_{opt} is the vector of optimization variables for stance phase; z_0 is the base's vertical initial position; $\alpha_{(1-4)}$ are the Bézier polynomial coefficients of ground reaction force; T_{st} is the total stance time; q is the vector of joint angles and \dot{q} is the vector of joint velocities at all the sampling points.

Equality constraints were imposed to satisfy forward kinematics:

$$rot(q_1) \begin{bmatrix} l \\ 0 \end{bmatrix} + rot(q_1 + q_2) \begin{bmatrix} l \\ 0 \end{bmatrix} + \begin{bmatrix} 0 \\ z \end{bmatrix} = 0 \quad (2.9)$$

$$J(q)\dot{q} + \begin{bmatrix} 0 \\ \dot{z} \end{bmatrix} = \begin{bmatrix} 0 \\ 0 \end{bmatrix} \quad (2.10)$$

where $rot \in SO(2)$ is the rotation matrix. z and \dot{z} are the vectors of height

and velocity of the base at each sampling point using Equation 2.4.

MATLAB's *fmincon* function was used to search for local optimal solutions. The parameters for the knee extensor model is chosen as follows: mass $M = 0.66 \text{ kg}$, link length $l = 0.12 \text{ m}$. 100 simulation runs were executed over 10 different maximal motor speed (ω_{max} from 23 rad/s to 37 rad/s) and maximal torque (τ_{max} from 6.2 Nm to 9.7 Nm) constraints, then the maximal achievable height h_{max} is plotted as the third axis against τ_{max} and ω_{max} . As shown in Figure 2.2, the maximal achievable height increases as the upper limit for speed and torque increases. The level curves shows that h_{max} could reach as high as 0.8 m theoretically with the effective actuator torque of 9.7 Nm and actuator speed of 37 rad/s.

The advantage of this method is that it decoupled the study of jumping to two decoupled problems. In terms of dynamics, it treats the leg as a point mass accelerated due to ground reaction force and gravity; in terms of kinematics, it assumes two link kinematics chain for leg topology. After imposing equality constraints which bridges the error between kinematics as shown in Equations 2.9 and Equation 2.10, the problem is tackled in a way that avoids the problem of singularity in the search of optimization variables.

2.1.4 Admissible Operating Region

In general, Admissible Operating Region (AOR) is defined as the area in the torque-speed plane enclosed by the Leg's torque-speed trajectory in performing certain task, as is shown in Figure 2.3. The motions corresponding to the enclosed AOR region are admissible to the actuator. It is a projection of dynamic motion to the torque-speed domain of the actuators. It is a lumped quantity which treats the motor and gearbox as a unity instead of separating the characteristics of both. The contribution of the proposition of AOR is that it captures the essence of robot motion generation, and bridges between motor dynamics, and workspace dynamics. Furthermore, it could be used in the early stage of design by projecting workspace dynamics to actuator's speed-torque space, before the choice of motor and transmission design is determined.

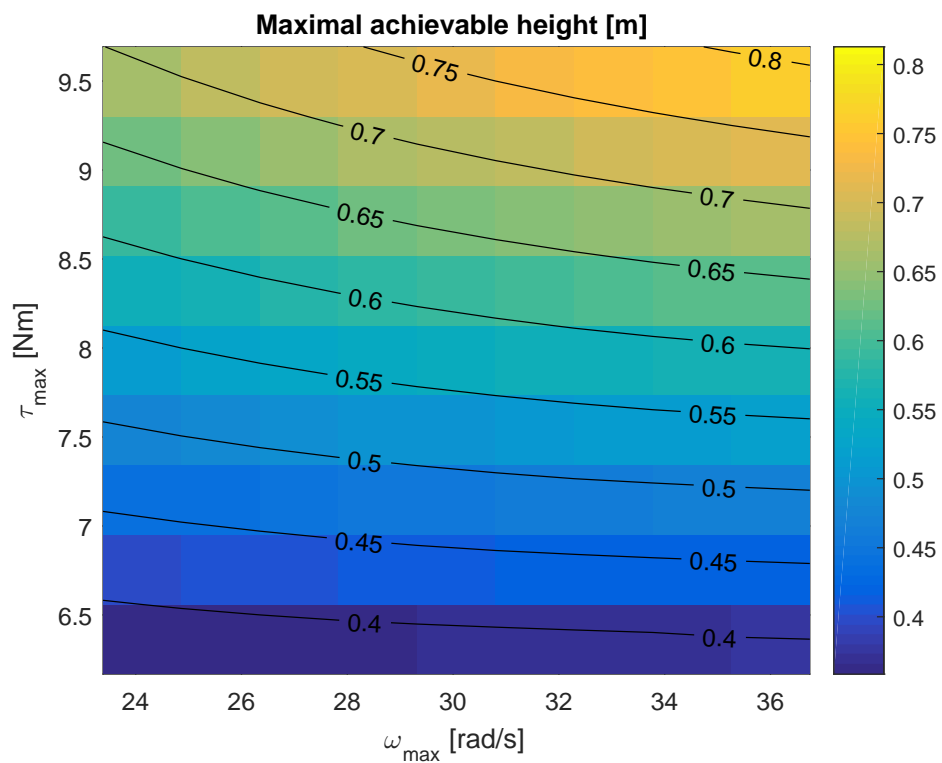


Figure 2.2: Maximal achievable height for specific torque and speed limit. The x-axis corresponds to maximal angular velocity of the actuator, the y-axis corresponds to maximal torque of the actuator, and the depth represents the maximal achievable height of a jump

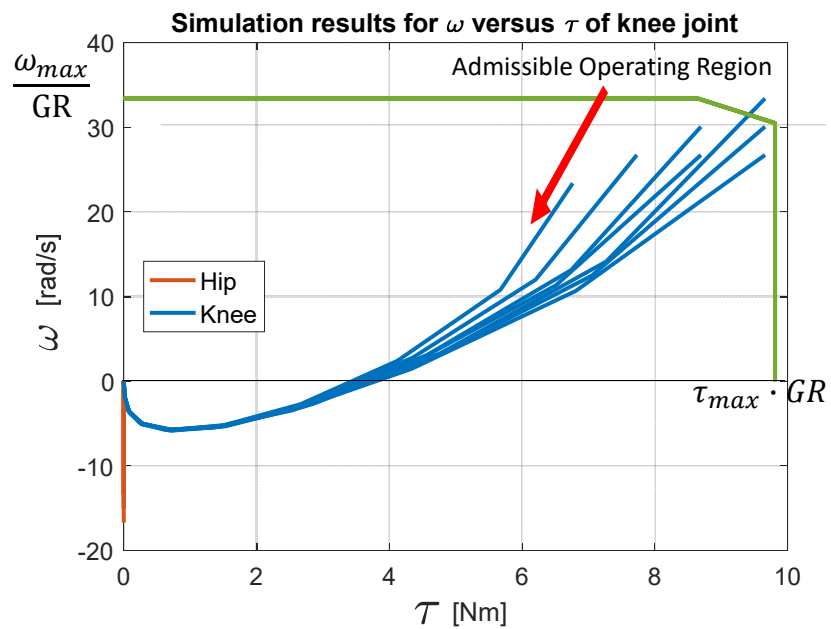


Figure 2.3: The Admissible Operating Region (AOR) formed by the torque and angular speed trajectories from the one hundred knee extensor model simulations. A typical motor's speed-torque curve scaled by gear ratio of 23:1 is plotted in green curve. Hip motor acts as a passive joint throughout the jumping up phase.

Scaling Effect of Gear Ratio

The analysis of AOR takes motor and gearbox as a whole entity. Since AOR is determined by desired motion, it does not change with gear ratio, hence it is independent of actuator and gearbox choices. What the gear ratio could scale is the motor characteristic curve. Shown as the green curve in Figure 2.3, the original speed-torque curve of this specific motor is scaled by gear ratio to enclose more of the AOR. Namely, the maximal motor speed ω_{max} is scaled down to ω_{max}/GR , and the maximal motor torque τ_{max} is multiplied to $\tau_{max}GR$. Geometrically speaking, the motor characteristic curve has become lower and wider.

Zero Torque at the Hip Joint

Multiple simulation results from Section 2.1.3 is plotted in Figure 2.3 shown as blue curves. Note that the torque requirement for Hip motor shown in red line is always zero. This result conforms to our formulation of the Knee Extensor Model, which assumes the foot is located directly below the hip point.

CHAPTER 3

SENSITIVITY ANALYSIS

3.1 Poincaré Map

3.2 Periodic Orbits

Periodic orbit is a special type of trajectories, where its initial and final states are identical. Mathematically speaking, periodic orbits could be expressed in the following manner:

$$x(t_0 + T) = \Phi(t, x_0, T)x(t_0) \quad (3.1)$$

where x is the state vector, T is called the period of the trajectory, t_0 is the initial time, and x_0 is the initial state. Equation 3.1 illustrates that the given initial state and period, the state after a period T should be the same as the initial state, hence the name periodic.

3.3 Monodromy Matrix

A linear mapping exists between the final state and initial state within a period, which is the $\Phi(t, x_0, T)$ matrix in equation 3.1. It has an official name as the Monodromy matrix. The idea of monodromy matrix is that it characterizes how perturbation in the initial state will propagate into the final state. So its eigenvalues indicate the stability of the dynamical system. When the eigenvalues lie within the unit circle in the complex plane, we could conclude that the system is stable, when the eigenvalues lie outside of the unit circle, we could conclude that the system is unstable.

Note that monodromy matrix could not only be used to analyze periodic

orbits, but also non-periodic dynamical systems. But when it was used to analyze periodic orbits, it is also known as the linearized Poincaré map.

3.3.1 Monodromy Matrix for LTI system

A Linear Time Invariant (LTI) system is one that evolves according to the following equations:

$$\dot{x}(t) = Ax(t) + Bu(t) \quad (3.2)$$

$$y(t) = Cx(t) + Du(t) \quad (3.3)$$

where A,B,C,D are constant matrices, $x(t)$ is the evolving state, $u(t)$ is the input vector and $y(t)$ is the output of the system. For a LTI system, the state transition matrix is:

$$\Phi(t, t_0) = e^{A(t-t_0)} \quad (3.4)$$

CHAPTER 4

DESIGN PRINCIPLES FOR DYNAMIC LEGGED ROBOTS

4.1 Transmission Design

The actuator design philosophy is to make high power actuators with the capability of interacting with the environment. Namely, the actuator should not be stiff as the heavily geared motors, which are widely used in industrial robots. Instead, it should be back-drivable meaning that the torque applied at the output shaft should be felt at the input shaft. The benefits are threefold, firstly, back-drivability prevents gearboxes from being damaged by external forces; second, it allows for proprioceptive sensing[20]; thirdly, allows for fast dynamics in legged locomotion.

After the motor selection and gear ratio is determined from previous sections, focus was put on how to design the transmission system so that it can achieve the desired gear ratio while satisfying dimensional constraints.

4.1.1 Transmission Design Comparison

Harmonic drive is composed of the wave generator, flexspline and circular spline. It could provide high gear ratio typically between 30:1 to 200:1 with zero backlash. Harmonic drive is employed by the quadrupedal robot starlETH[11] and the bipedal robot ATRIAS[10]. However, harmonic drive is not back-drivable, which contradicts with our design paradigm.

Cycloidal gearbox has very low backlash and high torsional stiffness. It can operate quietly and withstand shock load. Bipedal robot Cassie uses cycloidal gearbox as the transmission. The drawback of cycloidal gearbox is that it requires customizing high precision parts.

Single stage planetary gearbox has high efficiency and the load could be distributed between planet gears, and standard gears are widely available

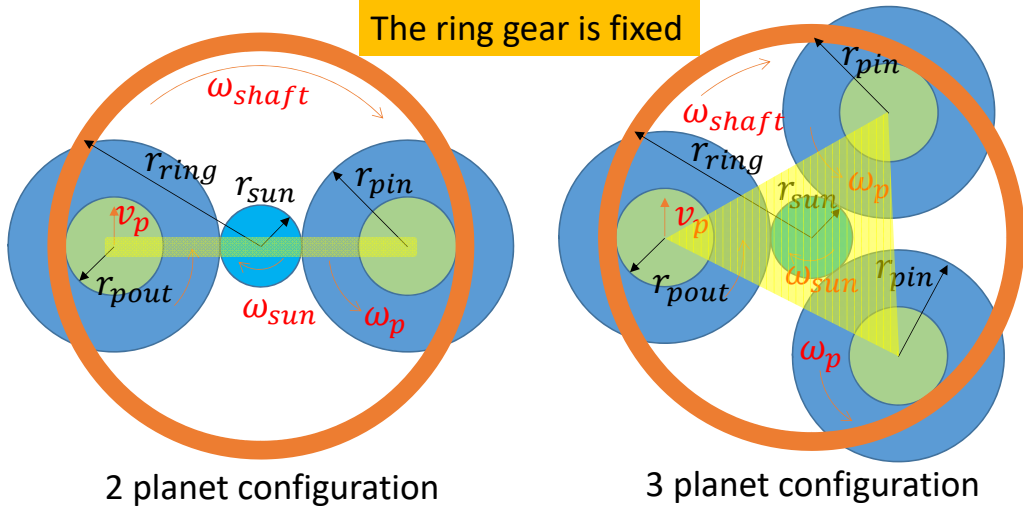


Figure 4.1: Schematics of Compound Planetary Gearbox Configurations. (left) 2 planet configuration, (right) 3 planet configuration

at low cost. Nevertheless, no gear combination could provide the desired gear ratio for the given dimensional limitation with pitch of 0.4.

Compound planetary gearboxes have the benefits of single stage planetary gearboxes while providing more compact design for there are two stages for the planet gear. There are a range of gear teeth selection for the given dimensional limits. It is adopted as the transmission system design considering the dimensional limit and gear ratio requirement of the motor design.

4.1.2 Compound Planetary Gearbox Design

The objective of compound planetary gearbox design is to achieve desired gear ratio within dimensional constraints imposed by motor selection. In order to derive the gear ratio for given gear teeth number, a schematics of the two-stage compound planetary gearbox is used as shown in Figure 4.1. For given gear teeth numbers, both configurations in Figure 4.1 are equivalent. Some assumptions for this analysis is posed here:

1. The sun gear located at the center is the input.
2. The output shaft shown as yellow transparent shape is the output.
3. The output shaft is connected to the axes of all the planet gears.

4. The sun gear is meshed with input planet gears.
5. The ring gear is meshed with output planet gears.
6. The ring gear is fixed.

Velocity equivalence is used to calculate the gear ratio.

$$\omega_{sun}r_{sun} = v_p + \omega_p r_{pin} \quad (4.1)$$

$$v_p = \omega_p r_{pout} \quad (4.2)$$

$$\omega_p = \frac{\omega_{sun}r_{sun}}{r_{pout}+r_{pin}} \quad (4.3)$$

$$\omega_{shaft} = \frac{\omega_p r_{pout}}{r_{sun}+r_{pin}} \quad (4.4)$$

where ω_{shaft} is the angular velocity of the output shaft and the rest of the variable definitions could be found in Table 4.1.

Therefore, the gear ratio of a compound planetary gearbox could be formulated as:

$$GR = \frac{\omega_{sun}}{\omega_{shaft}} = \frac{(r_{pout} + r_{pin})(r_{sun} + r_{pin})}{r_{sun}r_{pout}} = \frac{(N_{pout} + N_{pin})(N_{sun} + N_{pin})}{N_{sun}N_{pout}} \quad (4.5)$$

The planetary gearbox shown in Figure 5.1 utilizes two-stage compound planet gears to provide desired gear ratio while satisfying the dimensional constraints imposed by motor selection.

The constraints for choosing teeth numbers are listed as follows:

1. The teeth number of sun gear (N_{sun}) and ring gear (N_{ring}) could both be divided by the number of planet gears.
2. The pitch circles of sun gear and planet gears, as well as that of planet gears and the ring gear should be externally tangent,
i.e. $r_{ring} = r_{sun} + r_{pin} + r_{pout}$ or $N_{ring} = N_{sun} + N_{pin} + N_{pout}$.

Table 4.1: Variable Definition for Gear Ratio Calculation

	Sun gear	Input planet	Output planet	Ring gear
Pitch diameter	r_{sun}	r_{pin}	r_{pout}	r_{ring}
Angular velocity	ω_{sun}	ω_p	ω_p	N/A
Linear velocity	N/A	v_p	v_p	N/A
Teeth number	N_{sun}	N_{pout}	N_{pout}	N_{ring}

3. The gear ratio GR should be within the range of 22 - 25.
4. The radius of the gearbox should be less than 25 mm,
i.e. $\text{Max}[r_{ring}, r_{sun} + 2r_{pin}] < 12.5\text{mm}$
5. The teeth number for sun gear N_{sun} should be no less than 6. Other wise the meshing would be problematic because the profile of gear teeth would be distorted too much.

On top of the constraints, some practical issues were also considered in choosing gear teeth. Ideally, the phase difference between two stages of the planet gears should be the same. However, in compound gear manufacturing, the phase differnce could not be well maintained. To solve this problem, the planet gear teeth combination was chosen to be 16/53, which only share the common factor of 1. This choice provides tunable backlash with 2.1° increment in the gearbox assembly. This is very similar to the working principle of a mechanical caliper, which uses two scales (main scale and vernier scale) with small difference to achieve high precision.

A large number of teeth combinations were enumerated taking into account all the constraints. The optimal gear teeth choice emerged as $N_{sun} = 12$; $N_{pin} = 53$; $N_{pout} = 16$; $N_{ring} = 81$ and the gear ratio is 23.3594.

All gears are custom made by *HPC Gears Ltd* with 0.4 pitch and pressure angle of 20° .

4.2 Leg Topology Comparison

The full leg module will have three degrees of freedom (DOF) in order to achieve agile 3D maneuver. Three leg topologies, namely, open-serial chain, parallel five-bar and symmetric five-bar are analyzed in terms of workspace, force production and proprioceptive sensing. For simplicity, the abduction/adduction (ABAD) DOF is neglected and only motion in the 2-D hip-knee plane is analyzed. The analysis is based on the linkage analysis of Minitaur[13], but extended its analysis to negative δ value. Also, radial and lateral force, velocity and proprioceptive sensitivity are the three main concern in this section. In this section, all the analysis is based on the assumption of massless links, that is, no linkage mass or inertia is considered. This is

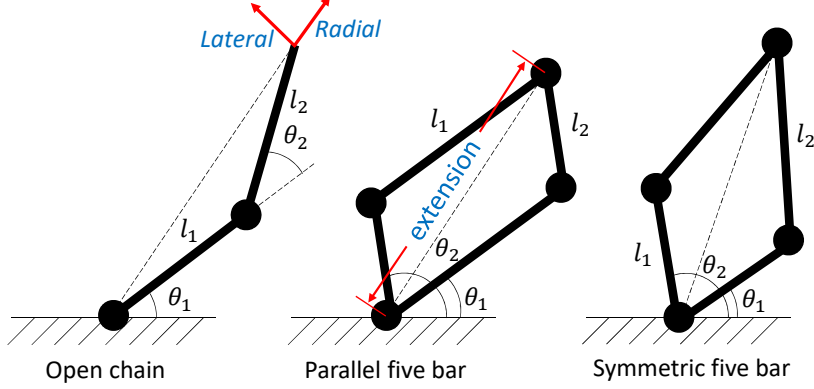


Figure 4.2: Three typical linkage topologies (a)Open-serial chain (b)Parallel five-bar (c)Symmetric five-bar. The design variable is δ and the workspace variable is the leg's radial extension

valid in real application because the majority of mass is taken by actuators, which could be placed at the base of the link and transmit power via some kind of power transmission system like linkage, chain or belt. Therefore, linkage mass is relatively light compared to the body or even less than 10% of the total mass, as shown in the MIT Cheetah design[9].

4.2.1 Workspace

For the three candidate leg topologies shown in Figure 4.2, the workspace is an annulus, which could be characterized by maximum radius r_{max} and minimum radius r_{min} of the annulus. The design space is defined as:

$$\delta = \frac{r_{min}}{r_{max}} \quad (4.6)$$

where $r_{max} = l_1 + l_2$ and $r_{min} = l_1 - l_2$, and l_1, l_2 are the lengths of the first and second links shown in Figure 4.2. Notice that here $\delta \in (-1, 1)$, which means l_1 should be either longer or shorter than l_2 , which serves as an extension to the analysis presented in [13].

4.2.2 Sweep Volume

For quadrupedal robot application, sweep volume is also another important factor to consider in linkage design. Large sweep volume is not desirable

because the four limbs of a quadrupedal robot are close to each other and the workspace would be decreased if the sweep volume is large. In addition, when interacting with unstructured terrain, large sweep volume increases the possibility of tripping and colliding. For example, when a robot is climbing upstairs, the leg sweep volume should stay clear of the stairs to avoid collision. In out door environment where there are debris and fabric that could easily tangle the robot, a slimmer and compact leg design would be more advantageous. Hence minimized sweep volume is favorable for quadrupedal robot leg design.

4.2.3 Force Production

Manipulability ellipsoids are used to characterize a robot arm's ability to move in certain configuration[14]. In the following sections, manipulability ellipsoids of force production, velocity production and proprioceptive sensitivity are utilized to present a manipulator's mechanical performance.

Force production ellipsoid characterizes how unit joint torque from motors will reflect as end-effector forces. Solution to equation 4.7 forms the Force production ellipsoid. The major and minor axes of the force production ellipsoid represent the end-effector's strongest and weakest ability to produce force at the respective directions.

$$E_{force} := \{F | F^T J J^T F = ||\tau||, ||\tau|| = 1\} \quad (4.7)$$

Radial/Lateral force production is defined as the end-effector force in radial/lateral directions given unit joint torque input. Figure 4.4 4.5 4.6 show how force production ability changes over *extension* and δ .

4.2.4 Velocity Production

Velocity production ellipsoid characterizes how unit joint velocity from motors will reflect as end-effector velocity. Solution to equation 4.8 forms the velocity production ellipsoid. The major and minor axes of the velocity production ellipsoid represent the end-effector's strongest and weakest ability to produce velocity at the respective directions.

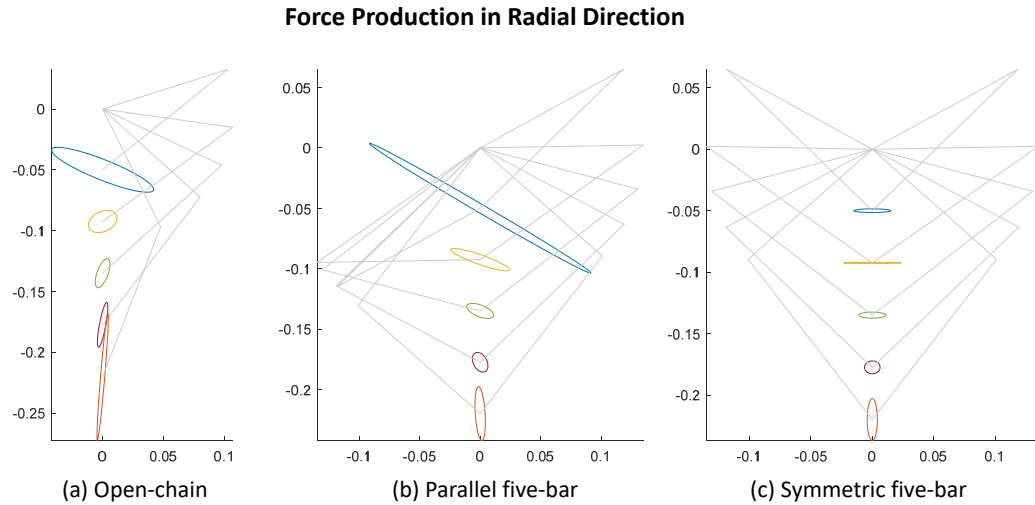


Figure 4.3: Force production in radial direction for an example linkage design of Open-chain, Parallel five-bar and Symmetric five-bar

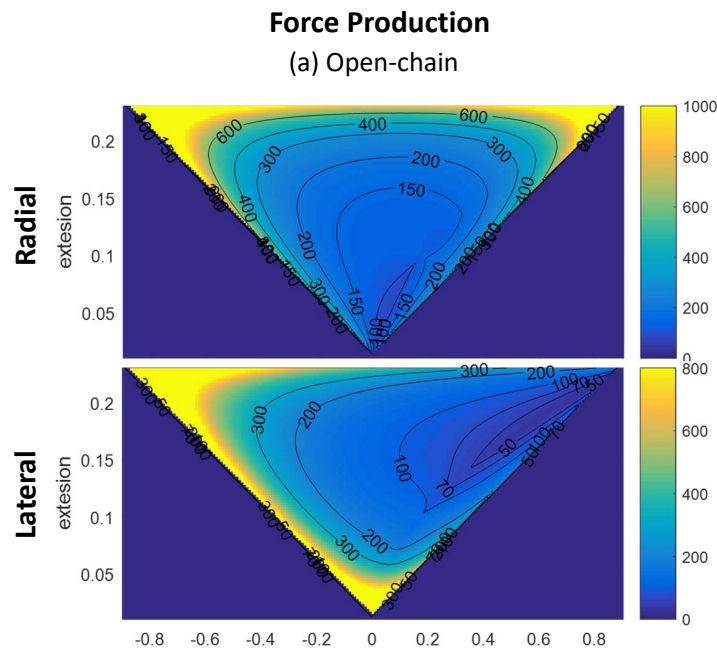


Figure 4.4: Force production in radial and lateral directions for open chain design

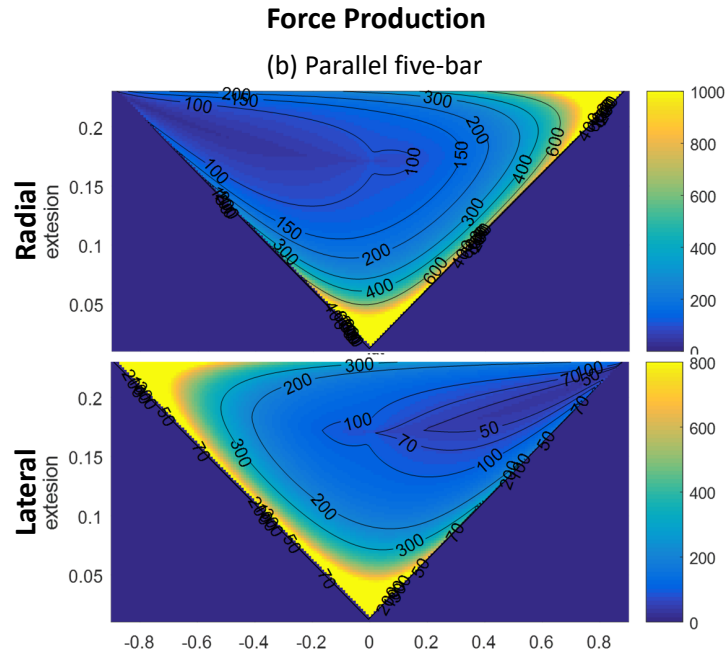


Figure 4.5: Force production in radial and lateral directions for parallel five-bar design

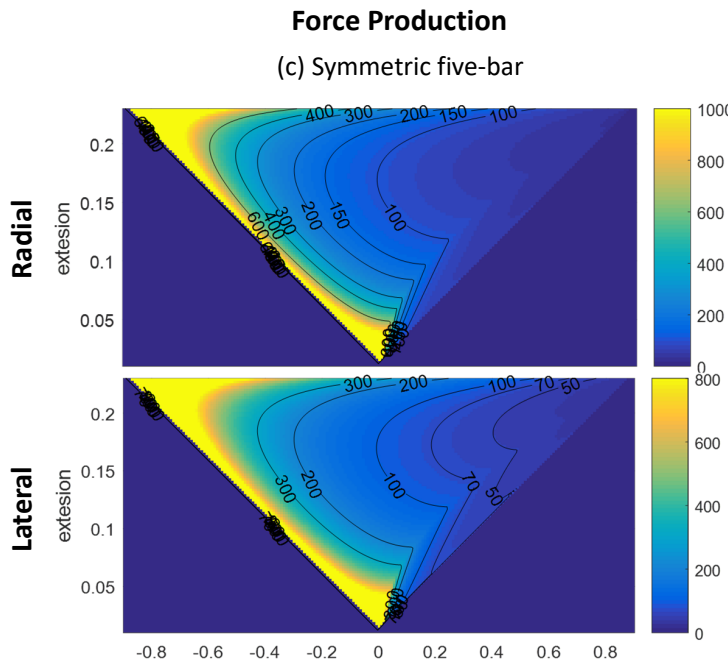


Figure 4.6: Force production in radial and lateral directions for symmetric five-bar design

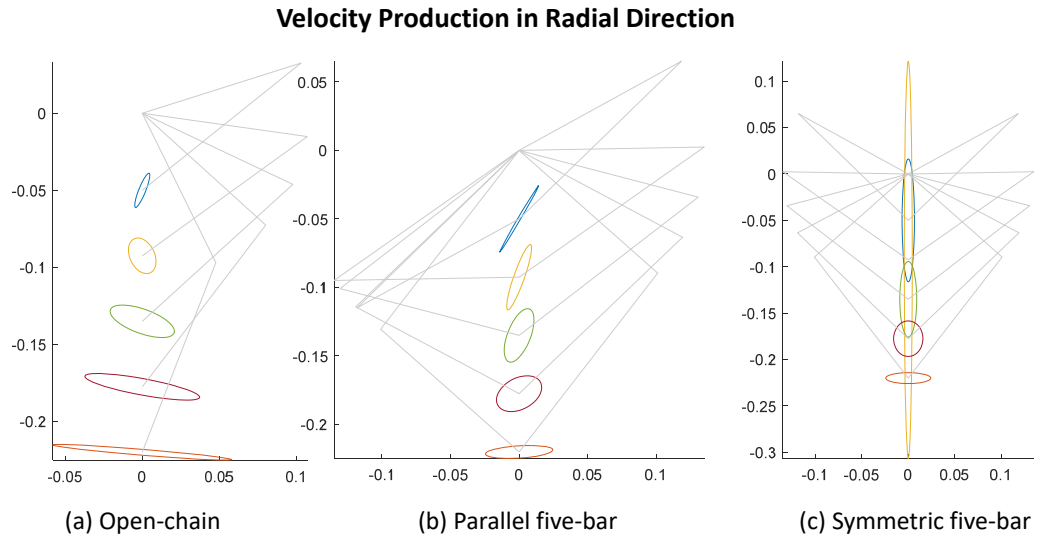


Figure 4.7: Velocity production in radial direction for an example linkage design of Open-chain, Parallel five-bar and Symmetric five-bar

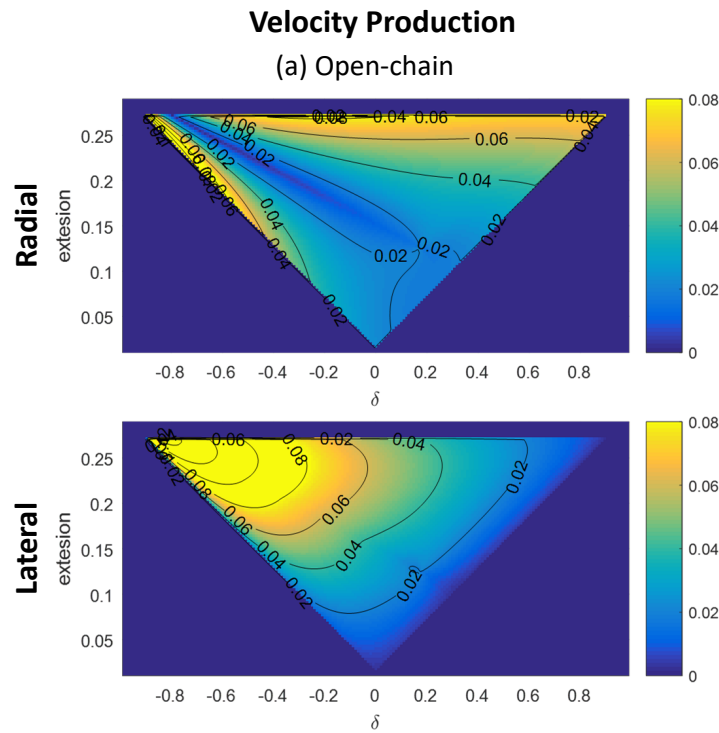


Figure 4.8: Velocity production in radial and lateral directions for open chain design

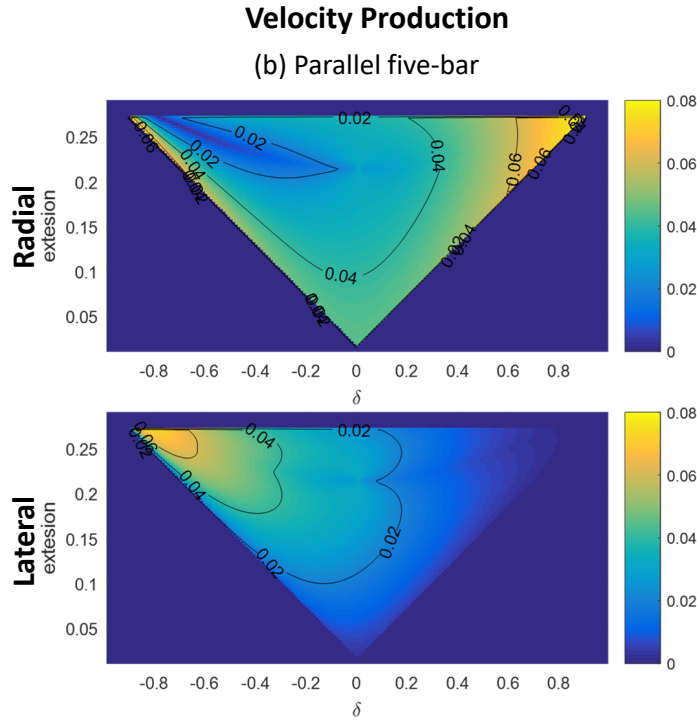


Figure 4.9: Velocity production in radial and lateral directions for parallel five-bar design

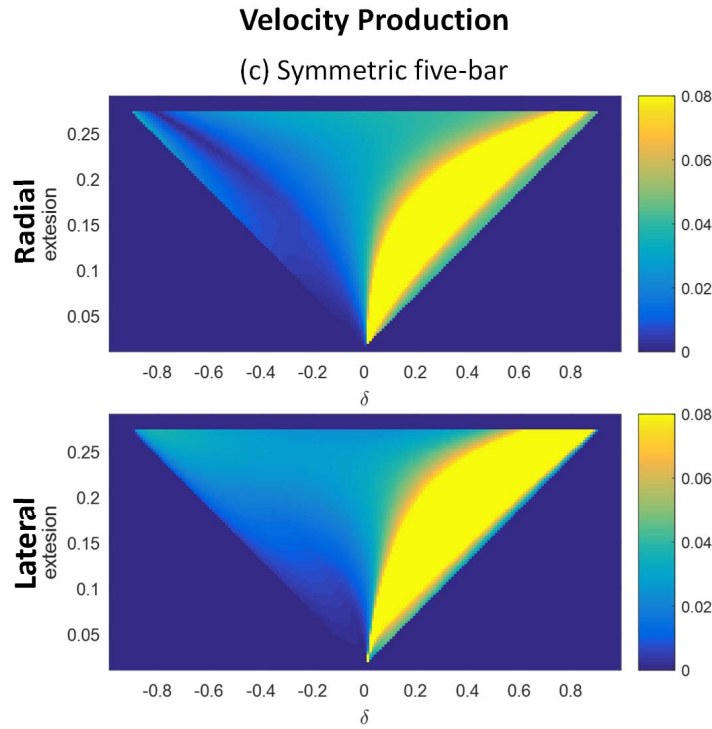


Figure 4.10: Velocity production in radial and lateral directions for symmetric five-bar design

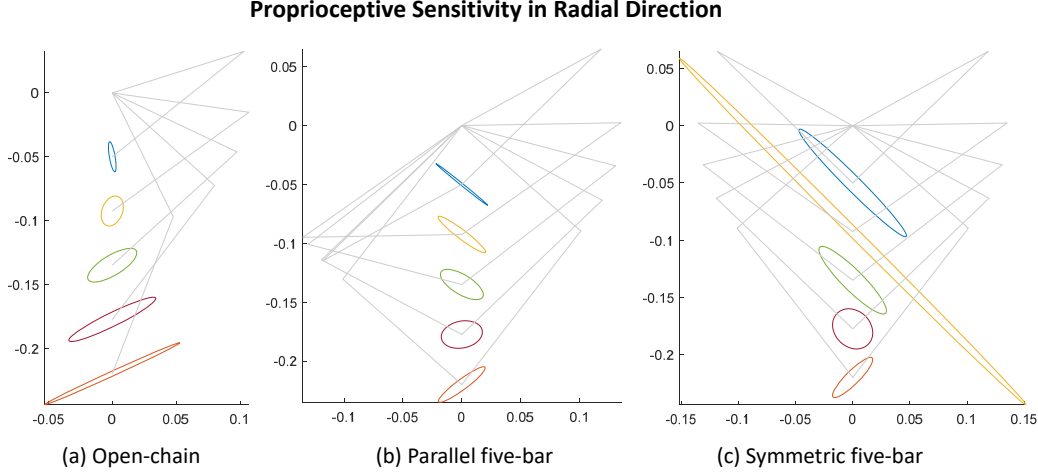


Figure 4.11: Proprioceptive Sensitivity in radial direction for an example linkage design of Open-chain, Parallel five-bar and Symmetric five-bar

$$E_{velocity} := \{V | (J^{-1}v)^T (J^{-1}v) = \|\omega\|, \|\omega\| = 1\} \quad (4.8)$$

Radial/Lateral velocity production is defined as the end-effector velocity in radial/lateral directions given unit joint angular velocity input. Figure 4.4 4.5 4.6 show how velocity production ability changes over *extension* and δ .

4.2.5 Proprioceptive Sensing

Proprioceptive sensitivity ellipsoid represents how unit force applied at the end-effector is visible to the motors. Solution to equation 4.9 forms the proprioceptive sensitivity ellipsoid.

$$E_{sensitivity} := \{\tau | \tau^T J^{-1} J^{-T} \tau = \|F\|, \|F\| = 1\} \quad (4.9)$$

An example linkage design for the thee leg topologies is shown in Figure 4.11 where design parameter δ is fixed as 0.1 and workspace parameter *extension* is varied. The figure shows that in this specific example, the area enclosed by proprioceptive sensitivity ellipsoid is almost the same with symmetric five-bar slightly better.

It is worth remarking that similar to force and velocity production, proprioceptive sensitivity should not only be considered in the radial direction, but also in the lateral direction. Radial/Lateral Proprioceptive Sensitivity

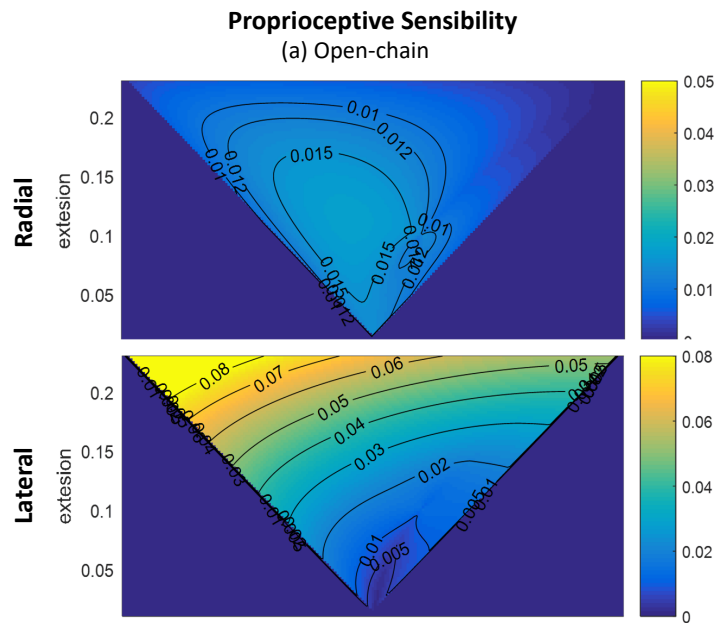


Figure 4.12: Proprioceptive Sensitivity in radial and lateral directions for the open-chain design

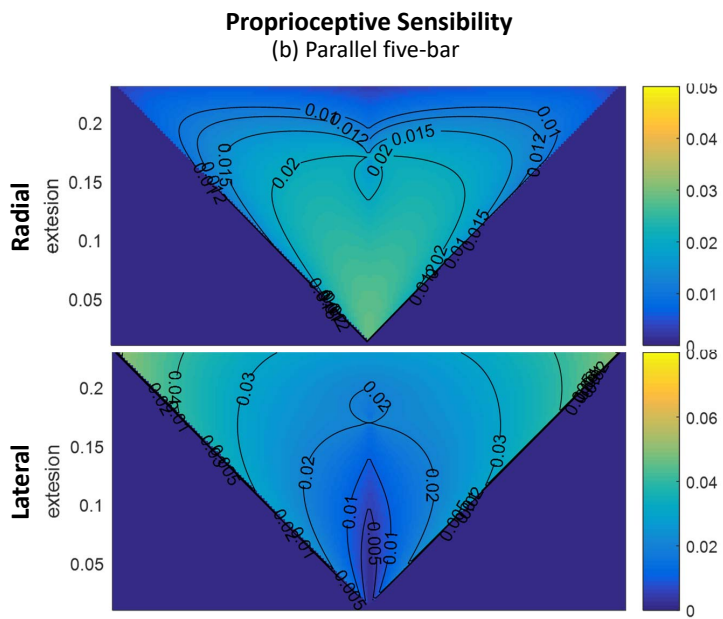


Figure 4.13: Proprioceptive Sensitivity in radial and lateral directions for the parallel five-bar design

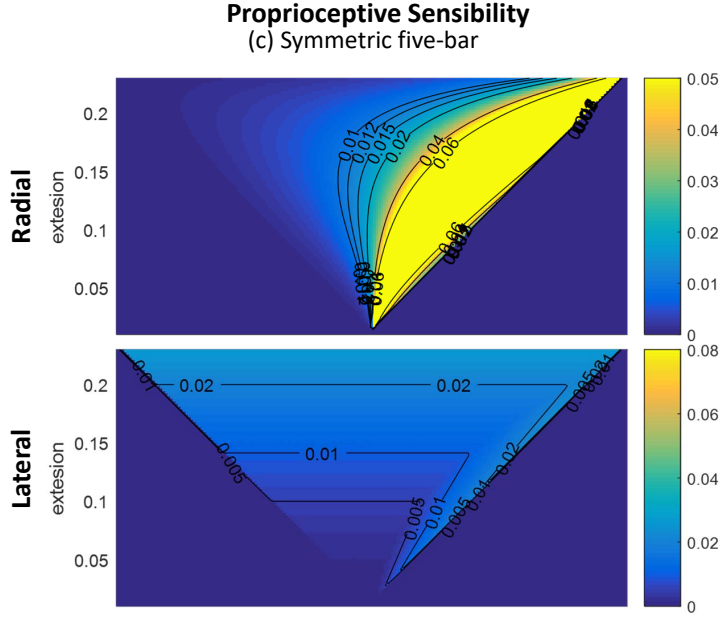


Figure 4.14: Proprioceptive Sensitivity in radial and lateral directions for the symmetric five-bar design

is defined as the joint torque magnitude when radial/lateral unit force is applied at the end-effector. Figure 4.12, 4.13, 4.14 show how proprioceptive sensitivity changes over design parameters *extension* and workspace variable δ .

Figure 4.12, 4.13, 4.14 show that while symmetric five-bar has excellent radial proprioceptive sensitivity, its lateral sensitivity is relatively poorer. In contrast, Open-chain design has better lateral proprioceptive sensitivity. Higher lateral sensitivity renders open-chain design advantageous in controlling horizontal forces, which is useful in applications such as jumping forward to precise location, control horizontal speed in running and so on.

4.2.6 Power Delivery

Since the velocity and force ellipsoids have their major axis coincide with the other's minor axis and vice versa, this means they are conjugate of each other. Thus the power delivery in every direction of the linkage design is assumed to be the same. But the manipulator analysis is static so only fixed instances are considered.

4.2.7 Linkage Design

Although symmetric five-bar has excellent velocity production ability in both radial and lateral directions, its proprioceptive sensitivity in lateral direction is not very good. In addition, both parallel and symmetric five-bar design suffer from too large sweep volume, which is not desirable for quadrupedal robot locomotion, especially in unstructured terrain. Therefore, open-chain topology is chosen to be the linkage design.

The previous sections have provided a recipe to come up with suitable link design for specific applications. An optimal design could be found by defining a cost function that pertains to application requirements.

$$Cost = -(w_{F_r}F_r + w_{F_l}F_l + w_{V_r}V_r + w_{V_l}V_l + w_{S_r}S_r + w_{S_l}S_l) + w_\delta\delta \quad (4.10)$$

where $F_r, F_l, V_r, V_l, S_r, S_l$ are the force production and δ is as defined before, velocity production and proprioceptive sensitivity values in the radial and lateral directions, which is **normalized** by the average value in the span of *extension* to get rid of the effect of magnitude of unit. $w_{F_r}, w_{F_l}, w_{V_r}, w_{V_l}, w_{S_r}, w_{S_l}, w_\delta$ are weighting factors that corresponds to the values. Higher weight could be put on the value that plays an important role on the application. For example, if a robot is designed to perform mostly in situations where high force production is required while operating in a low velocity region, the weighting factor for force production could be higher and the weighting factors for velocity production could be lower. By the same token, applications where precise force production is required could put higher penalty on the proprioceptive sensitivity term.

In this application we want to place a balanced emphasis on all the radial and lateral parameters, hence $w_{F_r}, w_{F_l}, w_{V_r}, w_{V_l}, w_{S_r}, w_{S_l}$ was all set to be equal, and w_δ was set to be 100 times larger than the other weighting factors to prevent optimal point appear at the infeasible region. The final optimized result showed that δ is very close to zero, which indicates that equal length link is favorable for leg topology.

CHAPTER 5

HARDWARE INTEGRATION

5.1 Mechanical Design of The Leg

With actuator from *section* and linkage design from *section*, this section presents a detailed mechanical design layout of the leg. The leg module is composed of three motor modules(HIP/KNEE/ABAD), each has a motor coil and a planetary gearbox with moderate gear ratio to achieve the Quasi-Direct-Drive[1] strategy. To accommodate size limitation imposed by actuator choice, the two-stage compound planetary gearbox is used as the transmission. The leg is design to optimize for large workspace, with the novel HIP-KNEE connection design, the knee joint could rotate 360°, the curved upper link and hollow thigh link design also enables large knee joint workspace.

5.1.1 HIP-KNEE Connection Design

Each leg module is composed of three brush-less DC (BLDC) motor modules. HIP, KNEE, ABAD stand for hip joint, knee joint and abduction/adduction joints respectively. The HIP and KNEE motors are placed face-to-face and coaxially as shown in Figure 5.2. Double supported by two thin-section bearings (KMF: PBXS020/ PBXS015), the KNEE motor could rotate 360° with respect to the HIP motor. One bearing (KMF: PBXS015) is located between HIP and KNEE motors and the other one (PBXS020) is located outside of the HIP motor shell and enclosed by two hip caps. An explosive view could be found in Figure 5.3. The HIP motor shell's outer surface is used as one of bearing PBXS020's mating surface, and the inner surface of the Hip cap is used as the other mating surface. The hip cap is fixed to the KNEE motor and grips on the HIP motor via PBXS020 bearing, allowing

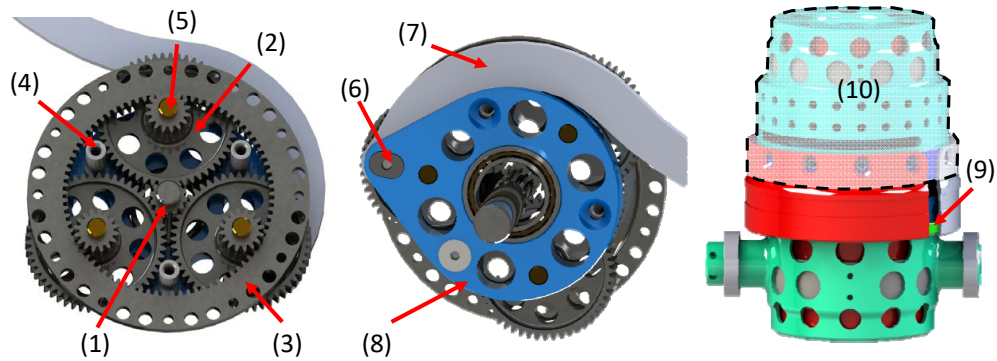


Figure 5.1: Planetary gearbox design with three compound planet gears (left); curved upper-link design (middle); hip and knee motor module (right); (1) sun gear, (2) compound planet gear, (3) ring gear, (4) stand-off, (5) brass dowel pin, (6) output pin, (7) upper link, (8) KNEE carrier, (9) KMF PBXS020 bearing, (10) the KNEE motor module

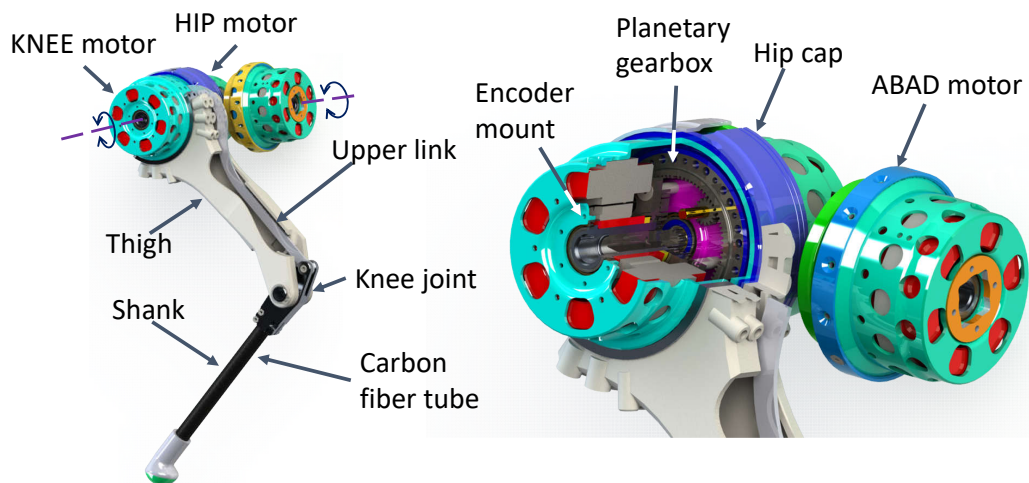


Figure 5.2: CAD Model of the Leg Module Design; (left) A side-view of the leg module with cut-out on thigh link showing the four-bar linkage design; (right) A cut-out view showing the internal structure of a motor module

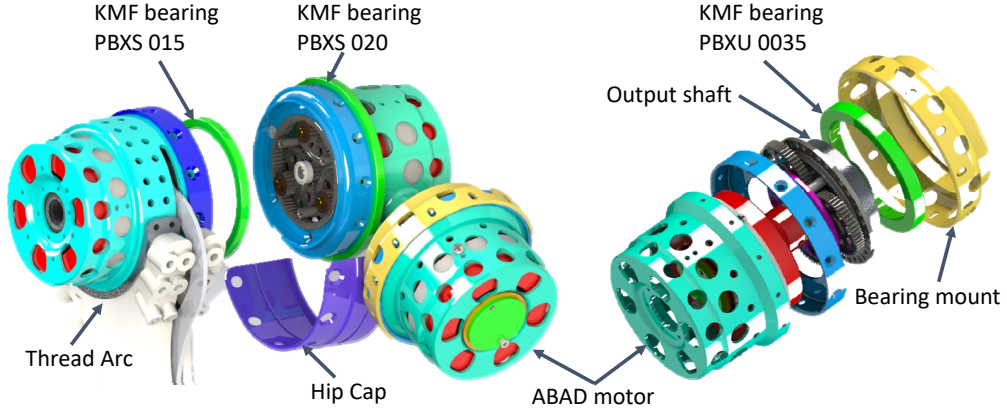


Figure 5.3: (left) Connection Design Between HIP and KNEE Motors for Large Hip Range of Motion (ROM); (right) Exploded View of ABAD motor

the KNEE motor to rotate freely related to the HIP motor.

The ABAD motor's rotational axis is placed perpendicular to the HIP/KNEE motors' axis. The internal structure of the ABAD motor is shown in Figure 5.3. The torque produced by electrical coil is magnified by the planetary gearbox and transferred to the output shaft, whose motion is constrained by the bearing mount via another thin-section bearing(KMF PBXU0035). The output shaft of ABAD motor is directly connected to the HIP/KNEE module. With transmission eliminated, the workspace of the ABAD joint is not limited by the leg itself.

5.1.2 Linkage Transmission Design

The linkage transmission design is shown in Figure 5.2. The torque of the KNEE motor is transmitted to the knee joint through a four-bar linkage mechanism. Hence the KNEE motor could be put nearer to the main body and the rotary inertia could be reduced. The 3D printed hollow thigh design allows the curved upper link to travel inside without interference, while providing protection to the upper link. Consequently, the robot-human interface would be safer. In addition, the curved upper link design allows larger knee joint workspace compared with straight link design As shown in Figure 5.1, the curved link avoids the standoff (4) in the figure and gains 27° more rotation angle compared with straight four-bar linkage design.

The thigh link was connected to the KNEE motor surface through four

screws initially. During preliminary jumping tests it turned out that the large ground impact impulse at touch down would rip off the thread on the KNEE motor shell. To solve this problem, an additional part called thread arc was made to provide more threaded holes on the knee motor. Figure 5.3 shows that the thread arc is attached to the KNEE motor surface and the new thigh link is fixed to the thread arc with 18 screws to evenly distribute the load.

5.1.3 Electronic System Integration

The electronic system of the robot leg consists of the following components: two Elmo Gold Twitter amplifiers were used for motor commutation, two RLS-RMB20 magnetic encoders were used to measure motor angle, ATI Mini40 F/T sensor was used to measure the ground reaction force created by the leg. The control loop runs at 4kHz on an Intel i5 desktop in Simulink Real-Time.

REFERENCES

- [1] S. K. O. 2016, “Design for 3D Agility and Virtual Compliance Using Proprioceptive Force Control in Dynamic Legged Robots,” no. October, 2016.
- [2] R. Alexander, “McN.(1992) exploring biomechanics. animals in motion,” *Scientific American Library, New York*, vol. 247.
- [3] H. Asada and K. Youcef-Toumi, *Direct-drive Robots: Theory and Practice*. Cambridge, MA, USA: MIT Press, 1987.
- [4] M. F. Bobbert, M. R. Yeadon, and B. M. Nigg, “Mechanical analysis of the landing phase in heel-toe running,” *Journal of Biomechanics*, vol. 25, no. 3, pp. 223–234, 1992.
- [5] C. Carignan and K. Cleary, “Closed-loop force control for haptic simulation of virtual environments,” *Haptics-e*, vol. 1, no. 2, pp. 1–14, 2000. [Online]. Available: <https://haptics-e.org/>
- [6] Ç. Disibüyük and H. Oruç, “A generalization of rational bernstein–bézier curves,” *BIT Numerical Mathematics*, vol. 47, no. 2, pp. 313–323, 2007.
- [7] E. H. Doha, A. H. Bhrawy, and M. A. Saker, “Integrals of Bernstein polynomials: An application for the solution of high even-order differential equations,” *Applied Mathematics Letters*, vol. 24, no. 4, pp. 559–565, 2011. [Online]. Available: <http://dx.doi.org/10.1016/j.aml.2010.11.013>
- [8] R. J. Full, D. E. Koditschek, and R. J. Full, “Templates and anchors: neuromechanical hypotheses of legged locomotion on land,” *The Journal of Experimental Biology*, vol. 2, no. 12, pp. 3–125, 1999.
- [9] S. K. Hae-Won Park¹, Patrick M. Wensing², “High-Speed Bounding with the MIT Cheetah 2: Control Design and Experiments,” *Journal of Animal Science*, pp. 1–11, 2015. [Online]. Available: <http://arxiv.org/abs/1508.04886>
- [10] C. Hubicki, J. Grimes, M. Jones, D. Renjewski, A. Spröwitz, A. Abate, and J. Hurst, “ATRIAS: Design and Validation of a Tether-Free 3D-Capable Spring-Mass Bipedal Robot,” *The International Journal*

- of Robotics Research, vol. 35, no. 12, pp. 1497–1521, 2016. [Online]. Available: <http://ijr.sagepub.com/content/35/12/1497.abstract>
- [11] M. Hutter, “StarlETH & Co-design and control of legged robots with compliant actuation,” *ETH Zürich*, vol. PhD Thesis, no. 21073, 2013. [Online]. Available: <http://e-collection.library.ethz.ch/view/eth:7183>
 - [12] S. Kalouche, “Design for 3d agility and virtual compliance using proprioceptive force control in dynamic legged robots,” Ph.D. dissertation, CARNEGIE MELLON UNIVERSITY, 2016.
 - [13] G. Kenneally, A. De, and D. Koditschek, “Design Principles for a Family of Direct-Drive Legged Robots,” *IEEE Robotics and Automation Letters*, vol. 1, no. 2, pp. 900–907, 2016.
 - [14] K. M. Lynch and F. C. Park, “Introduction To Modern Robotics Mechanics, Planning, and Control,” p. 408, 2016.
 - [15] H. W. Park, S. Park, and S. Kim, “Variable-speed quadrupedal bounding using impulse planning: Untethered high-speed 3D Running of MIT Cheetah 2,” *Proceedings - IEEE International Conference on Robotics and Automation*, vol. 2015-June, no. June, pp. 5163–5170, 2015.
 - [16] D. W. Robinson, J. E. Pratt, D. J. Paluska, and G. A. Pratt, “Series elastic actuator development for a biomimetic walking robot,” in *Advanced Intelligent Mechatronics, 1999. Proceedings. 1999 IEEE/ASME International Conference on*. IEEE, 1999, pp. 561–568.
 - [17] Y. Sakagami, R. Watanabe, C. Aoyama, S. Matsunaga, N. Higaki, and K. Fujimura, “The intelligent ASIMO: system overview and integration,” *IEEE/RSJ International Conference on Intelligent Robots and System*, vol. 3, no. October, pp. 2478–2483, 2002.
 - [18] K. Schmidt-Nielsen, *Scaling: why is animal size so important?* Cambridge University Press, 1984.
 - [19] M. N. Scholz, M. F. Bobbert, and A. K. van Soest, “Scaling and jumping: Gravity loses grip on small jumpers,” *Journal of Theoretical Biology*, vol. 240, no. 4, pp. 554–561, 2006.
 - [20] S. Seok, A. Wang, D. Otten, and S. Kim, “Actuator design for high force proprioceptive control in fast legged locomotion,” *IEEE International Conference on Intelligent Robots and Systems*, pp. 1970–1975, 2012.
 - [21] R. M. Walter and D. R. Carrier, “Ground forces applied by galloping dogs,” *Journal of Experimental Biology*, vol. 210, no. 2, pp. 208–216, 2007. [Online]. Available: <http://www.ncbi.nlm.nih.gov/pubmed/17210958>